

Theoretical study of high harmonic generation in monolayer NbSe₂

Daniel A. Rehn,^{1,*} Towfiq Ahmed,² Jinkyoungh Yoo,³ Rohit Prasankumar,³ and Jian-Xin Zhu^{4,3,†}

¹*Computational Physics Division, Los Alamos National Laboratory, Los Alamos, New Mexico 87545, USA*

²*National Security Directorate, Pacific Northwest National Laboratory, Richland, Washington 99354, USA*

³*Center for Integrated Nanotechnologies, Los Alamos National Laboratory, Los Alamos, New Mexico 87545, USA*

⁴*Theoretical Division, Los Alamos National Laboratory, Los Alamos, New Mexico 87545, USA*

(Dated: February 28, 2025)

High harmonic generation (HHG) is a powerful probe of electron dynamics on attosecond to femtosecond timescales and has been successfully used to detect electronic and structural changes in solid-state quantum materials, including transition metal dichalcogenides (TMDs). Among TMDs, bulk NbSe₂ exhibits charge density wave (CDW) order below 33 K and becomes superconducting below 7.3 K. Monolayer NbSe₂ is therefore interesting as a material whose different structural and electronic properties could be probed via HHG. Here, we predict the HHG response of the pristine 2H and CDW phases of monolayer NbSe₂ using real-time time-dependent density functional theory under the application of a simulated laser pulse excitation. We find that due to the lack of inversion symmetry in both monolayer phases, it is possible to excite even harmonics and that the even harmonics appear as the transverse components of the current response under excitations polarized along the zigzag direction of the monolayer, while odd harmonics arise from the longitudinal current response in all excitation directions. This suggests that the even and odd harmonic response can be controlled via the polarization of the probing field, opening an avenue for potentially useful applications in opto-electronic devices.

INTRODUCTION

Transition metal dichalcogenides (TMDs) have attracted much attention recently for their useful and novel physical properties. [1, 2] In bulk form, most TMDs exist as stacked two-dimensional layers where the atoms within each layer exhibit strong covalent bonding and layers are held together by weaker van der Waals interactions. These bulk structures can be exfoliated down to a single layer (i.e., monolayer), and most TMD monolayers exhibit interesting properties not found in the bulk. Many monolayer TMDs exhibit structural polymorphism, in which the individual layers can exist in multiple structural phases that can be exploited for a variety of applications. [3] As such, monolayer TMDs are currently being investigated for a wide range of potential applications, such as their use in phase-change memory,[4–6] optoelectronics,[7] sensors, [8–10] straintronic devices,[2, 11] and more.

Several monolayer and bulk TMDs exhibit charge density wave (CDW) order and superconductivity at low temperatures, as seen in NbS₂, [12–16] NbSe₂, [17–36] TaS₂, [37–40] and TaSe₂, [41–44] making them potentially useful for controlling these quantum phases with external stimuli, not only in the form of temperature, but also with other non-thermal external stimuli such as electrostatic doping [35] and strain. [36]

In recent years, high harmonic generation (HHG) has been studied in the context of both bulk [45–52] and monolayer materials [53–62] with important applications. HHG has been used as a probe to detect the 2H-to-1T'

structural phase change in monolayer MoTe₂ upon electrostatic doping, [6, 63] topological phase transitions in WTe₂, [64] and to study harmonic orders of up to 13 in monolayer MoS₂. [65] In addition, recent experiments have shown the appearance and tunability of non-integer harmonics in the topological insulator Bi₂Te₃. [66] Such studies demonstrate the utility of HHG as a useful attosecond to femtosecond probe of a wide range of materials that can be used in a variety of applications.

In this work, we study the HHG of monolayer NbSe₂ using real-time time-dependent density functional theory (RT-TDDFT) simulations. By exciting the monolayer with a simulated terahertz femtosecond laser pulse, we can predict the current response and HHG spectra under a variety of pulse orientations and strengths, as the real-time propagation allows us to probe both the linear and nonlinear electronic response regimes. Doing so, we find that monolayer NbSe₂ exhibits a strong anisotropy in the strength of the transverse current response when excited along the [100] crystal axis (x or zigzag direction, oriented along the \mathbf{a} lattice constant in Fig. 1) and [010] crystal axis (y or armchair direction, perpendicular to \mathbf{a} in Fig. 1). [2] In the case of excitation along the armchair direction, we find that the even modes are largely suppressed for both the longitudinal (current parallel to pulse orientation) and transverse (current perpendicular to pulse orientation) current response. However, for laser pulses oriented along the zigzag direction, we find that the transverse components of the current response are strongly amplified for excitation strengths of 10^{11} and 10^{12} W/cm², well above the linear response regime.

In the case of excitation along the zigzag direction, the longitudinal HHG spectrum consists primarily of odd-numbered multiples of the excitation frequency ($n\omega_0$, $n = 1, 3, 5, \dots$ with ω_0 the laser pulse frequency). The in-

* rehnd@lanl.gov

† jxzhu@lanl.gov

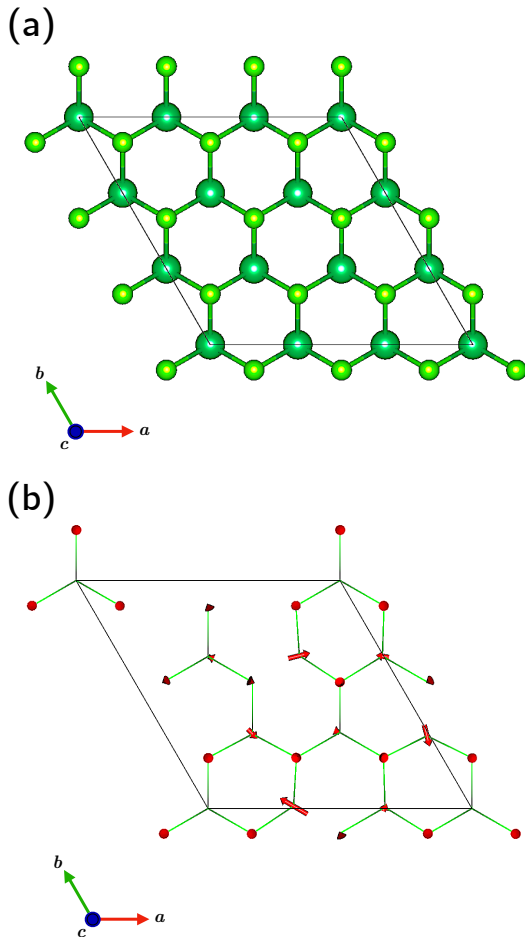


FIG. 1. Unit cell of (a) 2H monolayer and (b) a monolayer of the CDW phase, with arrows representing enlarged atomic distortion directions from the 2H monolayer. Nb atoms are dark green, Se atoms are light green. Simulations are performed for both cells shown, each of which consists of 27 atoms.

version symmetry breaking of the 2H monolayer, as compared to its 2H bulk form, allows in general for even modes ($n\omega_0$, $n = 2, 4, \dots$) to be present. We find that these even modes appear in the HHG spectra as the transverse components of the current for pulses oriented along the zigzag direction. In this sense, the transverse HHG spectra under excitation along the zigzag direction could be exploited for use in device applications. To summarize, the odd-numbered modes of the HHG response are present in excitations oriented along both the zigzag and armchair directions, but the even mode response occurs only for excitations along the zigzag direction, and in that case the even modes occur only in the transverse direction, so that the direction-dependence of both the exciting laser pulse and measurement orientation may be exploited.

In addition to the current response, we investigate the effect of CDW distortion on the HHG spectrum of mono-

layer NbSe₂. We find that the CDW distortion, determined from prior experiments, does not lead to an appreciable change in the HHG spectrum as compared to the pristine 2H monolayer. This is a result of the small atomic displacements of the CDW phase as compared to the 2H phase that lead to only small changes in the electronic structure of the CDW phase. To understand whether this would remain the case under larger distortions, we perform calculations under enlarged distortion conditions. We find that for these enlarged distortions, noticeable changes arise in the HHG spectra only when the ground state electronic structure changes appreciably from the 2H phase. This indicates the possibility that for materials exhibiting a larger structural change upon CDW formation than in NbSe₂, the pristine-to-CDW structural change could lead to distinct changes in the HHG spectra, opening the possibility of probing CDW distortion on femtosecond timescales.

RESULTS

Laser pulse excitation

Using the methodology discussed in the Methods section, we simulate the application of a femtosecond laser pulse for pulses polarized along both the zigzag armchair directions with a pulse shape whose Cartesian component $\alpha = x, y$ is defined as

$$A_\alpha(t) = -c \frac{E_o}{\omega_o} \cos(\omega_o t) \sin^2\left(\frac{\pi t}{\tau}\right) \Theta(\tau - t), \quad (1)$$

where the electric field can alternatively be defined as:

$$\begin{aligned} E_\alpha(t) &= -\frac{1}{c} \frac{\partial A_\alpha(t)}{\partial t} \\ &= \frac{E_o}{\omega_o} \frac{\partial}{\partial t} \left[\cos(\omega_o t) \sin^2\left(\frac{\pi t}{\tau}\right) \Theta(\tau - t) \right]. \end{aligned} \quad (2)$$

In our calculations, we use a pulse-width of $\tau = 30$ fs and photon energy $\omega = 0.6$ eV ≈ 145 THz. The intensity of the pulse is related to the amplitude by $I \approx cE_o^2/8\pi$. This equality only holds for infinite unmodulated wave trains (not pulses), but the approximation can be used to determine a corresponding value for E_o in Eqs. 1-2, as described in Ref. 67. The external field $E_\alpha(t)$ pulse shapes for four different intensities, 10^9 , 10^{10} , 10^{11} , and 10^{12} W/cm², are shown in Fig. 2a.

Calculations for both CDW and non-CDW structures were performed for a 31 fs time-propagation using $\Delta t = 0.08 \hbar/E_H$ atomic units, or 1.935 attoseconds as the time step. This timestep was determined to give the same HHG spectrum as simulations run with $\Delta t = 0.02 \hbar/E_h$ (see Supp. Material Sec. 4). For time-propagation, we used the enforced time-reversal symmetry propagator. [68] We also point out that there is a subtle issue associated with how to accurately extract HHG information from RT-TDDFT simulations that use periodic

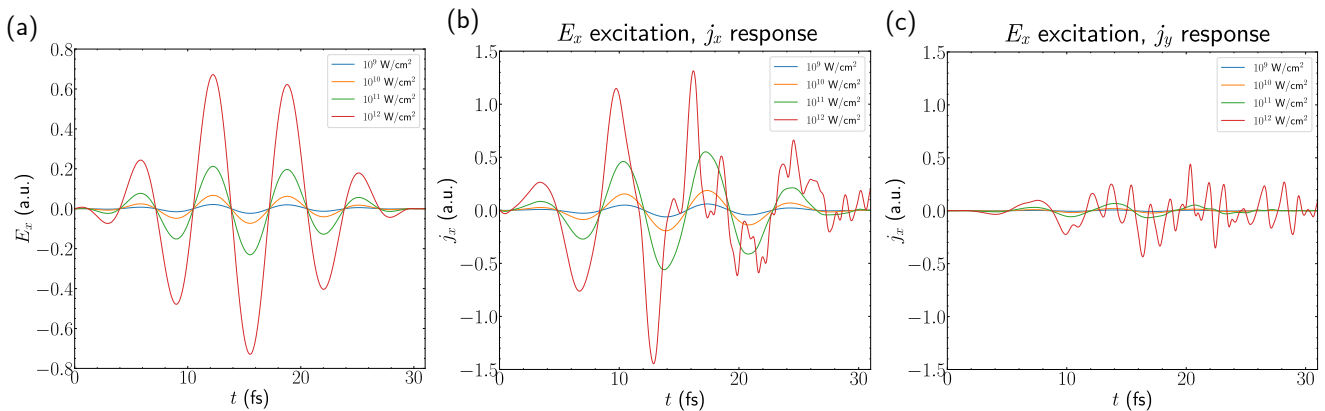


FIG. 2. Real-time excitation pulse and current response for excitations along the zigzag (E_x) direction, applied to the pristine 2H monolayer. (a) $E_x(t)$ for different pulse intensities, (b) Longitudinal current response $j_x(t)$ for different pulse intensities and (c) transverse current response (j_y) for different intensities.

boundary conditions. The issue that arises is that for long enough simulation times, the current can start to propagate through periodic repeats of the cell, which is unphysical and would not be seen experimentally. This issue so far has been addressed in two different ways. One is to use a multiscale modeling approach in which the microscopic current calculated in the RT-TDDFT approach is used as input to a macroscopic calculation that solves Maxwell's equations. [69, 70] The other approach is to run a normal RT-TDDFT simulation that is short enough to avoid the issue of the current interfering with its periodic repeats as a result of the application of periodic boundary conditions and a relatively small cell size. [71] Note that a related issue is ultrashort dephasing times. [72] Both approaches have been shown to produce useful qualitative information. Therefore, in this study we take the second approach and evolve the TDKS equations for only 1 fs after the 30 fs laser pulse. We extensively tested this issue and found that the results do not change much qualitatively for any total simulation time from 30-35 fs, as discussed in Supp. Material Sec. 6. We also point out that experimentally, HHG spectra are usually collected only for the duration of the excitation pulse, in agreement with our computational approach.

Transverse HHG in the 2H monolayer

With application of the electric field pulse described in Methods, we compute the current response throughout the pulse duration (30 fs) and for 1 fs after (31 fs total). As an example, we plot the longitudinal (j_x) and transverse (j_y) currents under excitation in the E_x direction in Fig. 2b and Fig 2c, respectively. This shows that the transverse components are much smaller in magnitude than the longitudinal current, though they are not negligible for the higher pulse strengths. In addition, we see a clear nonlinear response of the current after the

first ~ 10 fs for the 10^{12} W/cm 2 case, and although it is not as obvious for 10^{11} W/cm 2 , the nonlinear response is also present. By nonlinear, we mean that the current response does not respond linearly with the driving field and higher frequency oscillations in the current appear. The nonlinear transverse currents arise from the nonzero Berry curvature of bands. [73]

In Fig. 3 we plot the HHG spectra (calculated via Eq. 12) for the E_x (panel a) and E_y (panel b) excitations of the pristine 2H monolayer. The blue, orange, green, and red lines correspond to pulse intensities of 10^n W/cm 2 , $n = 9, 10, 11, 12$, respectively. The solid lines are the j_x current while the dashed lines are the j_y current. In panel a, the j_x current is the dominant contribution to the total current, being the longitudinal current response, whereas j_y is the dominant contribution for the E_y excitation, as in that case it is the longitudinal current. In addition, we see that in the 10^9 and 10^{10} W/cm 2 cases, the only prominent response is at the pulse frequency $\omega = \omega_0$. This is a clear indication that these pulse intensities are not strong enough to induce a nonlinear current response that is strong enough to observe a clear HHG signal. In contrast, we see that for pulse intensities of 10^{11} and 10^{12} W/cm 2 , we begin to see higher harmonics appear in the longitudinal current response for both E_x excitation (j_x response) and E_y excitation (j_y response). This indicates that these pulse intensities are strong enough to witness HHG.

In addition, we see that for the zigzag (E_x) excitation direction, the 10^{11} and 10^{12} W/cm 2 intensities give rise to a large j_y contribution, i.e., the transverse current response. In fact, for 10^{11} W/cm 2 , the second harmonic is nearly as strong as the fifth harmonic in j_x , and in the 10^{12} W/cm 2 case, the fourth harmonic is nearly as strong as the third harmonic in j_x . On the other hand, excitation in the armchair (E_y) direction does not lead to an appreciable transverse (j_x) response in any of the cases. For monolayers with space group $P\bar{6}m2$, no inversion symmetry is present, so it is possible to observe even

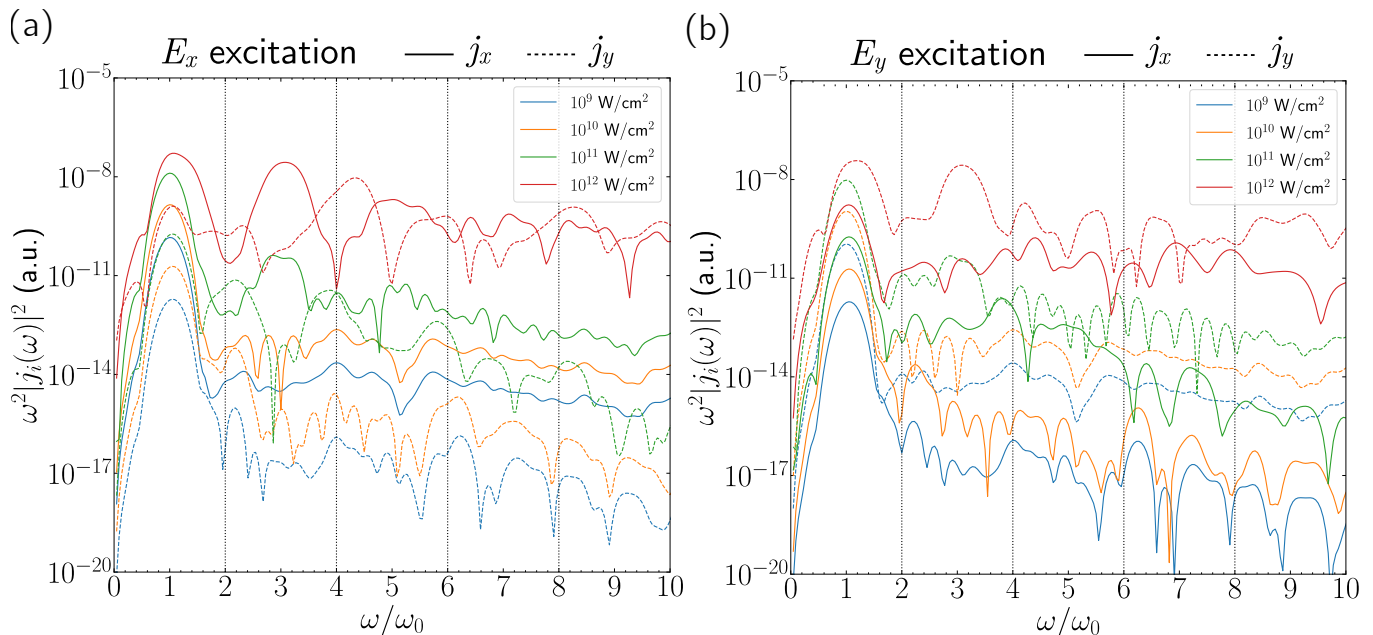


FIG. 3. HHG spectra for different excitation strengths in the 2H monolayer. (a) E_x excitation with j_x (solid) and j_y (dashed) response. (b) E_y excitation with j_x (solid) response and j_y (dashed) response.

harmonics in the HHG spectrum. This is in contrast to the bulk 2H phase, where an inversion center is present in the van der Waals gap between NbSe₂ layers.

One question is why we do not see a strong even harmonic response for excitation along the E_y direction. We first note that in fact, the even harmonics in j_y are not entirely absent in Fig. 3b. For example, we do see the 2nd harmonic in j_y for 10^{11} W/cm², and we see to some degree both the 2nd and 4th harmonics for 10^{12} W/cm². Nonetheless, the response is not strong. However, the symmetry considerations can only tell us whether a response is allowed or forbidden, and when allowed, the magnitude of response depends on the details of the underlying electronic structure, which must be computed.

The findings above indicate some potential optoelectronic device applications that we now discuss. Because even harmonics are only found for propagation along the [010] (or another symmetry-equivalent) direction, and because these even harmonics are only substantially excited for excitation pulses oriented along the [100] direction, it may be possible to use the even harmonic response as a femtosecond switch to pass information along. For example, given a large enough single-crystal monolayer, it would be possible to apply laser pulses oriented along different directions and simultaneously collect the response. Similar to bits that are either 0 or 1, the appearance of an even harmonic within some femtosecond or shorter window could represent a 1, and the non-appearance could represent a 0. If the pulse intensity were also used as an input variable, it could be possible to go beyond binary channels and pass information along 0 (no even harmonic), 1 (2nd harmonic), and 2 (fourth harmonic), etc. By constructing rules for how one type

of response (appearance of a particular harmonic) triggers subsequent excitations, a complex network of rules could be constructed to filter information on femtosecond timescales.

HHG in the CDW monolayer

Having explained the prediction of the transverse HHG response for even harmonics in the pristine 2H monolayer, we now turn to the question of how the HHG response of the CDW phase compares with that of the 2H monolayer. Using the same computational approach, we make comparisons of only the longitudinal current response in Fig. 4 (the transverse current responses are shown in Supp. Material Sec. 7). We include only the longitudinal current in order to more easily see the comparisons and reduce clutter in the figure. Clearly, the HHG spectra look extremely similar for both the pristine (dashed lines) and CDW (solid lines) phases. Although we do see some modest differences, particularly for the 10^{12} W/cm² case in panel b, these differences are likely not prominent enough to be useful for device applications. These findings are also true for the transverse HHG responses shown in Supp. Material Sec. 7, where again there are some noticeable differences in the 10^{12} W/cm² case, though they may not be large enough to clearly differentiate phases experimentally.

One interesting question that arises is why the CDW distortion does not lead to a significant change in the HHG properties. We point out that since the CDW phase also lacks inversion symmetry, the even harmonics may be present. For NbSe₂, the atomic displacements in

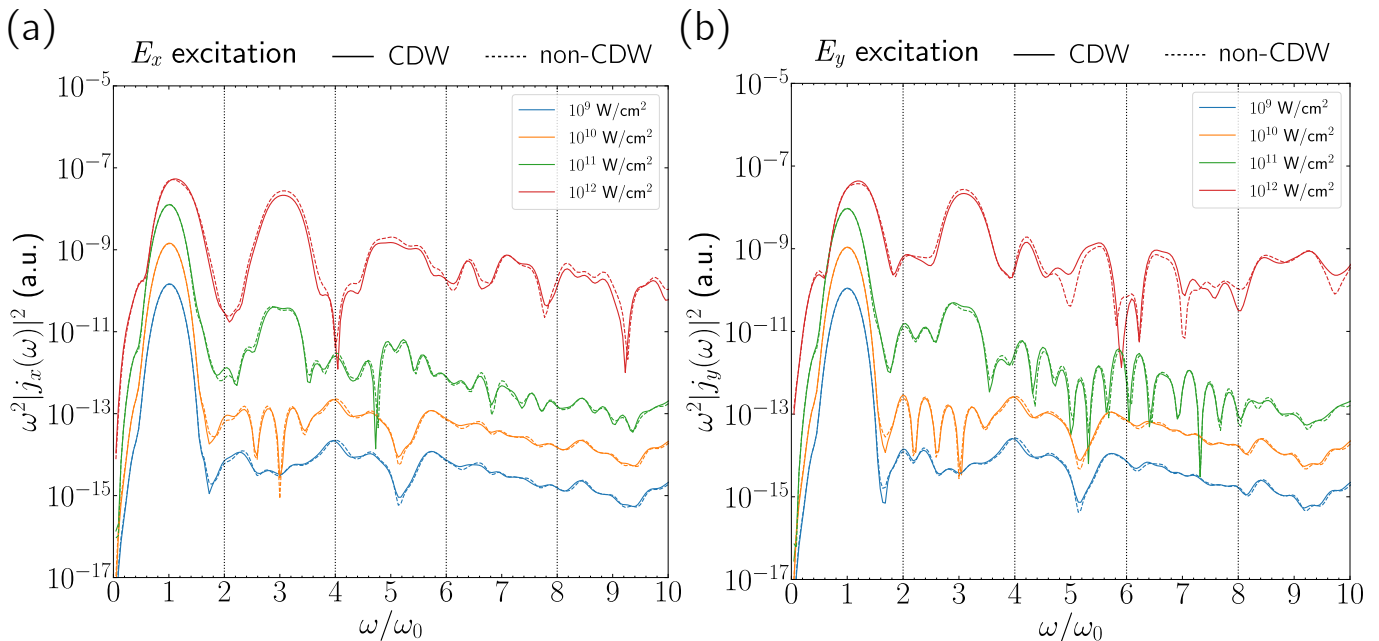


FIG. 4. Comparison of the longitudinal current HHG spectra for the CDW (solid lines) and 2H (dashed lines) cells at different pulse intensities. (a) E_x excitation with j_x response. (b) E_y excitation with j_y response. Only the longitudinal components are included in order to reduce clutter; the corresponding transverse components can be found in Supp. Material Sec. 7.

moving from the pristine to CDW phase are quite small and comparisons of the ground state electronic density of states (DOS) show that the distortions are not enough to significantly change the DOS. Although it is not *a-priori* clear that close agreement of the ground state DOS for the two phases is sufficient to say that the HHG spectra will be close, we find that this is borne out in our numerical simulations. However, it will be important to investigate this experimentally, as well.

Although we do not find significant differences in the HHG spectra for the CDW and pristine phases of NbSe₂, the case may be different for other materials with larger CDW structural changes. Therefore, one interesting question is whether a theoretically enlarged CDW distortion of the CDW phase of NbSe₂ could lead to differences in the HHG spectra. To explore this, we employ the following technique to generate CDW structures with enlarged distortions. Denoting the positions of the atoms in the pristine 9 f.u. 2H cell as \mathbf{r}_i^{2H} ($i = 1, 2, \dots, 27$) and the positions of atoms in the 9 f.u. CDW cell as \mathbf{r}_i^{CDW} ($i = 1, 2, \dots, 27$), we define a new set of atomic positions

$$\mathbf{r}_i^\alpha = \mathbf{r}_i^{CDW} + \alpha(\mathbf{r}_i^{CDW} - \mathbf{r}_i^{2H}). \quad (3)$$

This definition allows us to use different values of α to enhance the structural distortion, with $\alpha = 0$ corresponding to the experimental CDW structure. In Fig. 5 we present comparisons of the longitudinal HHG spectra for E_x and E_y excitations for $\alpha = 0, 2, 4$ in panels b and c, respectively. For the case of $\alpha = 4$, the distortion is large enough to start to see noticeable qualitative changes in the HHG spectra. This is also true for the transverse HHG spectra shown in Supp. Material Sec. 8, where we

see perhaps even larger qualitative changes to the HHG spectra.

The case of $\alpha = 4$ also produces a significant change in the ground state DOS as compared to the $\alpha = 0$ case, as seen in Fig 5a. Therefore, from the basis of these calculations, one indicator for whether we might expect to see qualitative changes in the HHG spectra of CDW and non-CDW phases of other materials is if their ground state DOS are significantly different. Of course, CDW distortions that lead to changes in space group, particularly in cases where an inversion symmetry is broken, could also be expected to lead to large qualitative differences in the HHG spectra. In this case, both $\alpha = 2, 4$ have space group $P\bar{6}$ (#174), which is a lower symmetry than the CDW phase and where inversion symmetry is again absent.

While we do not find it useful to discuss in detail the myriad of changes in the HHG signatures of the structures with enlarged distortions (since those structures would not be realized easily in experiments), the investigation shows that at least theoretically, CDW distortions can lead to distinct HHG spectra that could be detected experimentally and potentially exploited for device applications. Other materials that exhibit large structural distortions could therefore be interesting to explore both in simulations and experiments.

DISCUSSION

We have presented results from a computational study of laser pulse excitations of monolayer NbSe₂ in its pris-

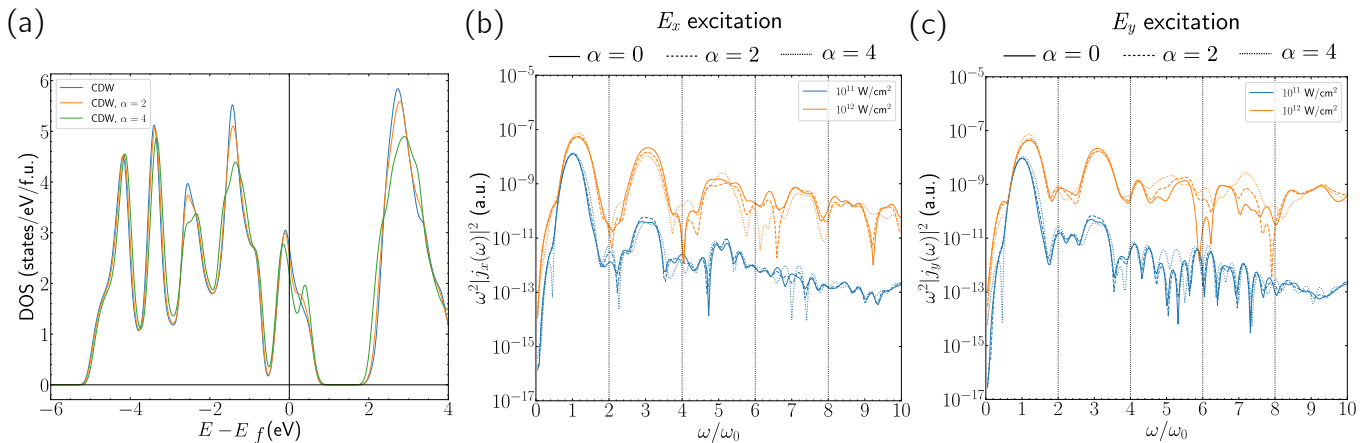


FIG. 5. (a) Ground state DOS for the CDW ($\alpha = 0$) and enlarged distortion ($\alpha = 2, 4$) structures. (b) Longitudinal HHG spectra for E_x excitation and j_x response and (c) Longitudinal HHG response for E_y excitation and j_y response, for 10^{11} (blue) and 10^{12} (orange) W/cm² pulse intensities for the three values of α .

tine 2H and CDW phases. Different pulse orientations and strengths lead to the following predictions: (1) the longitudinal current response for excitations along both the zigzag and armchair directions of NbSe₂ leads to an HHG signature that is dominated by odd harmonics for excitation strengths of $\sim 10^{11}$ W/cm² and higher; (2) the transverse HHG response is extremely pronounced in case of excitations along the zigzag direction and appear predominantly as even harmonics, whereas excitations along the armchair direction do not lead to such a prominent appearance of even harmonics in neither the longitudinal nor transverse HHG components; (3) the HHG response of the experimentally measured CDW phase does not reveal any significant changes from the pristine 2H phase, however (4) enlarging the CDW distortion leads to significant qualitative changes in the HHG spectra, indicating that other materials with larger CDW structural distortions than those of NbSe₂ may lead to distinct differences in HHG spectra.

The findings summarized here indicate some potential ways to exploit the findings for useful opto-electronic device applications. In particular, since the even harmonics only appear strongly as the transverse part of the current response for excitations along the zigzag direction, it may be possible to use the detection of even harmonics as a binary, ternary, or higher order switch to pass along information. The potential benefit for opto-electronic applications is that devices could be made atomically-thin and operate on femtosecond or faster timescales. Experimental investigation of the predictions presented here would shed light on the feasibility of using NbSe₂ or other materials for this, and other, device applications.

METHODS

The real-time formulation of time-dependent density functional theory [74] is carried out in a time-dependent Kohn-Sham (KS) scheme in which the KS wavefunctions $\psi_i(\mathbf{r}, t)$ are evolved via [75]

$$i\hbar \frac{\partial}{\partial t} \psi_i(\mathbf{r}, t) = \hat{H}_{\text{KS}} \psi_i(\mathbf{r}, t), \quad (4)$$

where i is the band index and

$$\begin{aligned} \hat{H}_{\text{KS}} = & \frac{\mathbf{p}^2}{2m} + v_{\text{ion}}(\mathbf{r}) + e^2 \int d\mathbf{r}' \frac{n(\mathbf{r}', t)}{|\mathbf{r} - \mathbf{r}'|} \\ & + v_{xc}[n(\mathbf{r}, t)] + e\mathbf{E}(t) \cdot \mathbf{r}. \end{aligned} \quad (5)$$

and $\mathbf{p} = -i\hbar\nabla$, m is the electron mass, and $v_{\text{ion}}(\mathbf{r})$ is the potential of the ions, assumed here to be static and treated using pseudopotentials as discussed below. The third term is the Hartree Coulomb interaction, the fourth term $v_{xc}[n]$ is the exchange-correlation potential, and the electron density is

$$n(\mathbf{r}, t) = \sum_i |\psi_i(\mathbf{r}, t)|^2. \quad (6)$$

$\mathbf{E}(t)$ is the time dependent electric field. The time-dependent external interaction potential term $e\mathbf{E}(t) \cdot \mathbf{r}$ breaks the translational symmetry of periodic systems. This can be addressed by adopting the velocity gauge, where a vector field, defined as [69]

$$\mathbf{A}(t) = -c \int^t \mathbf{E}(t') dt', \quad (7)$$

is used to gauge-transform the KS wave functions as [76]

$$\psi(\mathbf{r}, t) \rightarrow \exp\left[\frac{ie}{\hbar c} \mathbf{A}(t) \cdot \mathbf{r}\right] \psi(\mathbf{r}, t). \quad (8)$$

The velocity gauge TDKS Hamiltonian now takes the form

$$\hat{H}_{\text{KS}}^{\text{RT}} = \frac{1}{2m} \left[\mathbf{p} + \frac{e}{c} \mathbf{A}(t) \right]^2 + v_{\text{ion}}(\mathbf{r}) + e^2 \int d\mathbf{r}' \frac{n(\mathbf{r}, t)}{|\mathbf{r} - \mathbf{r}'|} + v_{xc}[n(\mathbf{r}, t)]. \quad (9)$$

The coupling to the external field is now incorporated in the kinetic energy term, and consequently the translational symmetry of the Hamiltonian is restored. The time-dependent KS orbitals are now evolved using

$$i\hbar \frac{\partial}{\partial t} \psi_i(\mathbf{r}, t) = \hat{H}_{\text{KS}}^{\text{RT}} \psi_i(\mathbf{r}, t). \quad (10)$$

In RT-TDDFT a time evolution propagator is needed to evolve Eq. 10 in time. Several options for doing so for solids have been discussed in the literature, [68, 77–79] with a detailed discussion found in Ref. 77.

By propagating the KS wave functions, the time-dependent current density

$$\mathbf{j}(t) = -\frac{i}{2\Omega} \int_{\Omega} d\mathbf{r} \sum_i [\psi_i^*(\mathbf{r}, t) \nabla \psi_i(\mathbf{r}, t) - \text{c.c.}] \quad (11)$$

can be obtained, whose power spectrum gives the HHG response

$$\text{HHG}(\omega) = \omega^2 \left| \int_0^T \mathbf{j}(t) \exp(-i\omega t) dt \right|^2. \quad (12)$$

Here Ω is the spatial volume of the unit cell and T in the Fourier transformation is the total propagation time for our simulation.

The velocity gauge formalism for RT-TDDFT has been implemented in several codes, including TDAP [80], RT-SIESTA, [81] Elk, [82, 83] OCTOPUS, [84] and SALMON, [85] among others. We used SALMON version 2.0.2 for all calculations presented in this article. SALMON is a real space code with options to apply periodic boundary conditions, so it is well-suited for studying monolayer NbSe₂.

All calculations are performed for fixed atomic positions, since the maximum simulation times are on the order of tens of femtoseconds, much faster than the vibrational timescales of the nuclei. In addition, all calculations are performed under the adiabatic approximation within TDDFT, which is to say that we neglect the history dependence in the evaluation of the exchange-correlation functional at each time and instead evaluate $v_{xc}[n]$ using the instantaneous $n(\mathbf{r}, t)$. Within the adiabatic approximation we employ the local density approximation (LDA) [86] for all calculations. SALMON makes use of pseudopotentials and for all calculations we use Trouiller-Martin type norm-conserving LDA-FHI pseudopotentials [87, 88] for the Nb and Se atoms, where 5 ($4d^4 5s^1$) and 6 ($4s^2 4p^4$) electrons were treated in the valence, respectively. We verified the accuracy of these

pseudopotentials for reproducing the ground state electronic structure of monolayer NbSe₂ by comparing the ground state density of states (DOS) to highly accurate all-electron calculations performed in the Elk code [83] version 7.0.12 (see Supp. Material Sec. 3 for details). The density of states we calculate is in good agreement with X-ray photoemission experiments. [89] Also note that we do not include spin orbit coupling (SOC) effects in this work, as this capability is not available in the code at present. SOC effects were studied recently in the context of the CDW phase. [90]

For all calculations we used hexagonal unit cells for both the pristine 2H monolayer and CDW monolayer that consist of 9 formula units (f.u.) of NbSe₂ (27 atoms in total). The pristine monolayer and CDW space groups are both $P\bar{6}m2$ (#187) within the standard tolerances of the symmetry software used. [91] The monolayer structures are found by isolating a single layer of the bulk 2H phase, space group $P6_3/mmc$ (#194), and CDW phase, space group $P6_3/m$ (#176). For the CDW phase, the 9 f.u. cell corresponds to the primitive cell, while for the 2H phase this corresponds to a $3 \times 3 \times 1$ supercell (see Fig. 1). In order to isolate the effects of CDW distortion in our calculations, we chose to use the same lattice constants for both the pristine and CDW phases, where we use the CDW phase lattice constants determined by Malliakas et al. (Ref. 21) measured at 15 K, which is $|a| = |b| = 10.3749$ Å. This corresponds to a primitive 2H unit cell size of $|a| = |b| = 3.4583$ Å, which is slightly expanded from the 2H lattice constants measured at room temperature, $|a| = |b| = 3.442$ – 3.446 Å, as determined by various sources. [21, 92] This corresponds to an axial strain of the pristine cell of less than 0.5%, not accounting for differences arising from thermal expansion. As NbSe₂ is metallic, the use of the bulk experimental lattice constants, which will in general not correspond exactly to the equilibrium (zero temperature) lattice constants of the monolayer predicted within the LDA, is not expected to lead to a significant qualitative change in the RT-TDDFT results. This situation would be different for semiconducting and insulating systems, in which small strains can lead to important qualitative changes that could strongly influence the current response, e.g., stemming from changes from a direct to indirect band gap. Because the monolayer lattice constants are not as well characterized and depend on the choice of substrate and growth or exfoliation method, we chose to use the experimentally measured bulk CDW lattice constants for all monolayer calculations.

All RT-TDDFT calculations require an initial calculation of the ground state as an initial state used to start the real time propagation with the laser pulse described above. Because SALMON is a real space code and we use periodic boundary conditions, we must ensure that both the ground state and the HHG spectra are converged with respect to the real-space grid size and k-mesh. For the ground state, we determined that a grid density $n_r = 2$ pts/bohr is necessary to ensure that the wave functions

are adequately represented on the grid (see Supp. Material Sec. 2 for details). Note that accurate ground state calculations required some adjustments in the mixing parameters of the Broyden scheme [93] (see Supp. Material Sec. 1 for details), and the self consistency cycle was stopped after $(\int_{\Omega} |n_i(\mathbf{r}) - n_{i-1}(\mathbf{r})| d^3r) / N_{\text{el}} < 10^{-10}$, where $n_j(\mathbf{r})$ is the charge density computed for the j th step in the selfconsistency cycle and N_{el} is the total number of valence states in the cell.

To determine the k-mesh size needed for calculations, we first ensured that the ground state density of states was converged with respect to k-mesh size and then performed convergence studies of the HHG spectra with respect to k-mesh size. We found that for the 9 f.u. cells a k-mesh of size $8 \times 8 \times 1$ is needed to ensure the HHG spectra are well converged (see Supp. Material Sec. 5 for details). Also note that no symmetry reductions of the k-mesh are used in calculations, so as not to enforce unwanted symmetries in the time-dependent Kohn-Sham wave functions.

ACKNOWLEDGEMENT

We thank Christos Maliakas for graciously providing us with the CDW phase crystal structure, as determined from the XRD measurements in Ref. 21.

This work was carried out under the auspices

of the U.S. Department of Energy (DOE) National Nuclear Security Administration under Contract No. 89233218CNA000001 and was supported by the LANL LDRD Program under the Project No. 20190026DR. We acknowledge the support by the Institutional Computing Program at LANL and NERSC, via the Center for Integrated Nanotechnologies, a DOE BES user facility, for computational resources.

DATA AVAILABILITY

All data supporting the findings of this study are available from the corresponding author upon a reasonable request.

AUTHOR CONTRIBUTIONS

D.R performed computations and D.R., T.A., and J.-X.Z. analyzed the data. J.Y. and R.P. participated in the discussion of results. J.-X.Z. designed the project and led the investigations, D.R. and T.A. designed the computational approaches. All authors contributed to the writing of the manuscript. Correspondence should be addressed to D.R. (rehnd@lanl.gov) and J.-X.Z. (jxzh@lanl.gov).

COMPETING INTERESTS

The authors declare no competing interests.

-
- [1] W. Choi, N. Choudhary, G. H. Han, J. Park, D. Akinwande, and Y. H. Lee, Recent development of two-dimensional transition metal dichalcogenides and their applications, *Materials Today* **20**, 116 (2017).
- [2] D. Akinwande, C. J. Brennan, J. S. Bunch, P. Egberts, J. R. Felts, H. Gao, R. Huang, J.-S. Kim, T. Li, Y. Li, *et al.*, A review on mechanics and mechanical properties of 2D materials—Graphene and beyond, *Extreme Mechanics Letters* **13**, 42 (2017).
- [3] S. Manzeli, D. Ovchinnikov, D. Pasquier, O. V. Yazyev, and A. Kis, 2D transition metal dichalcogenides, *Nature Reviews Materials* **2**, 1 (2017).
- [4] Y. Li, K.-A. N. Duerloo, K. Wauson, and E. J. Reed, Structural semiconductor-to-semimetal phase transition in two-dimensional materials induced by electrostatic gating, *Nature communications* **7**, 10671 (2016).
- [5] D. A. Rehn, Y. Li, E. Pop, and E. J. Reed, Theoretical potential for low energy consumption phase change memory utilizing electrostatically-induced structural phase transitions in 2D materials, *npj Computational Materials* **4**, 2 (2018).
- [6] Y. Wang, J. Xiao, H. Zhu, Y. Li, Y. Alsaid, K. Y. Fong, Y. Zhou, S. Wang, W. Shi, Y. Wang, *et al.*, Structural phase transition in monolayer MoTe₂ driven by electrostatic doping, *Nature* **550**, 487 (2017).
- [7] Q. H. Wang, K. Kalantar-Zadeh, A. Kis, J. N. Coleman, and M. S. Strano, Electronics and optoelectronics of two-dimensional transition metal dichalcogenides, *Nature nanotechnology* **7**, 699 (2012).
- [8] N. Joshi, T. Hayasaka, Y. Liu, H. Liu, O. N. Oliveira, and L. Lin, A review on chemiresistive room temperature gas sensors based on metal oxide nanostructures, graphene and 2d transition metal dichalcogenides, *Microchimica Acta* **185**, 1 (2018).
- [9] E. Lee, Y. S. Yoon, and D.-J. Kim, Two-dimensional transition metal dichalcogenides and metal oxide hybrids for gas sensing, *ACS sensors* **3**, 2045 (2018).
- [10] J. Ping, Z. Fan, M. Sindoro, Y. Ying, and H. Zhang, Recent advances in sensing applications of two-dimensional transition metal dichalcogenide nanosheets and their composites, *Advanced Functional Materials* **27**, 1605817 (2017).
- [11] W. Wei, Y. Dai, and B. Huang, Straintronics in two-dimensional in-plane heterostructures of transition-metal dichalcogenides, *Physical Chemistry Chemical Physics* **19**, 663 (2017).
- [12] M. Leroux, L. Cario, A. Bosak, and P. Rodiere, Traces of charge density waves in NbS₂, *Physical Review B* **97**, 195140 (2018).
- [13] M. Van Maaren and G. Schaeffer, Superconductivity in group V^a dichalcogenides, *Physics Letters* **20**, 131 (1966).
- [14] R. Yan, G. Khalsa, B. T. Schaefer, A. Jarjour, S. Rouvimov, K. C. Nowack, H. G. Xing, and D. Jena, Thickness dependence of superconductivity in ultrathin NbS₂, *Ap-*

- plied Physics Express **12**, 023008 (2019).
- [15] I. Guillamón, H. Suderow, S. Vieira, L. Cario, P. Diener, and P. Rodiere, Superconducting density of states and vortex cores of 2H-NbS₂, *Physical review letters* **101**, 166407 (2008).
- [16] J. Kačmarčík, Z. Pribulová, C. Marcenat, T. Klein, P. Rodière, L. Cario, and P. Samuely, Specific heat measurements of a superconducting NbS₂ single crystal in an external magnetic field: energy gap structure, *Physical Review B* **82**, 014518 (2010).
- [17] M. Marezio, P. Dernier, A. Menth, and G. Hull Jr, The crystal structure of NbSe₂ at 15 K, *Journal of Solid State Chemistry* **4**, 425 (1972).
- [18] D. Sanchez, A. Junod, J. Muller, H. Berger, and F. Levy, Specific heat of 2H-NbSe₂ in high magnetic fields, *Physica B: Condensed Matter* **204**, 167 (1995).
- [19] B. Riccò, Fermi surface and charge density waves in niobium diselenide, *Solid State Communications* **22**, 331 (1977).
- [20] T. Straub, T. Finteis, R. Claessen, P. Steiner, S. Hüfner, P. Blaha, C. Oglesby, and E. Bucher, Charge-Density-Wave Mechanism in 2H-NbSe₂: Photoemission Results, *Physical review letters* **82**, 4504 (1999).
- [21] C. D. Malliakas and M. G. Kanatzidis, Nb–Nb interactions define the charge density wave structure of 2H-NbSe₂, *Journal of the American Chemical Society* **135**, 1719 (2013).
- [22] K. Rossnagel, O. Seifarth, L. Kipp, M. Skibowski, D. Voß, P. Krüger, A. Mazur, and J. Pollmann, Fermi surface of 2H-NbSe₂ and its implications on the charge-density-wave mechanism, *Physical Review B* **64**, 235119 (2001).
- [23] W. Tonjes, V. Greanya, R. Liu, C. Olson, and P. Molinié, Charge-density-wave mechanism in the 2H-NbSe₂ family: Angle-resolved photoemission studies, *Physical Review B* **63**, 235101 (2001).
- [24] H. Suderow, V. Tissen, J. Brison, J. Martínez, and S. Vieira, Pressure Induced Effects on the Fermi Surface of Superconducting 2H-NbSe₂, *Physical review letters* **95**, 117006 (2005).
- [25] M. Johannes, I. Mazin, and C. Howells, Fermi-surface nesting and the origin of the charge-density wave in NbSe₂, *Physical Review B* **73**, 205102 (2006).
- [26] S. Borisenko, A. Kordyuk, V. Zabolotnyy, D. Inosov, D. Evtushinsky, B. Büchner, A. Yaresko, A. Varykhalov, R. Follath, W. Eberhardt, *et al.*, Two energy gaps and Fermi-surface “arcs” in NbSe₂, *Physical review letters* **102**, 166402 (2009).
- [27] M. Calandra, I. Mazin, and F. Mauri, Effect of dimensionality on the charge-density wave in few-layer 2H-NbSe₂, *Physical Review B* **80**, 241108 (2009).
- [28] F. Weber, S. Rosenkranz, J.-P. Castellan, R. Osborn, R. Hott, R. Heid, K.-P. Bohnen, T. Egami, A. Said, and D. Reznik, Extended Phonon Collapse and the Origin of the Charge-Density Wave in 2H-NbSe₂, *Physical review letters* **107**, 107403 (2011).
- [29] A. Soumyanarayanan, M. M. Yee, Y. He, J. Van Wezel, D. J. Rahn, K. Rossnagel, E. Hudson, M. R. Norman, and J. E. Hoffman, Quantum phase transition from triangular to stripe charge order in NbSe₂, *Proceedings of the National Academy of Sciences* **110**, 1623 (2013).
- [30] C. J. Arguello, S. P. Chockalingam, E. P. Rosenthal, L. Zhao, C. Gutiérrez, J. Kang, W. Chung, R. M. Fernandes, S. Jia, A. J. Millis, *et al.*, Visualizing the charge density wave transition in 2H-NbSe₂ in real space, *Physical Review B* **89**, 235115 (2014).
- [31] C. J. Arguello, E. P. Rosenthal, E. F. Andrade, W. Jin, P. Yeh, N. Zaki, S. Jia, R. J. Cava, R. M. Fernandes, A. J. Millis, *et al.*, Quasiparticle Interference, Quasiparticle Interactions, and the Origin of the Charge Density Wave in 2H-NbSe₂, *Physical review letters* **114**, 037001 (2015).
- [32] M. Leroux, I. Errea, M. Le Tacon, S.-M. Souliou, G. Garbarino, L. Cario, A. Bosak, F. Mauri, M. Calandra, and P. Rodiere, Strong anharmonicity induces quantum melting of charge density wave in 2H-NbSe₂ under pressure, *Physical Review B* **92**, 140303 (2015).
- [33] M. M. Ugeda, A. J. Bradley, Y. Zhang, S. Onishi, Y. Chen, W. Ruan, C. Ojeda-Aristizabal, H. Ryu, M. T. Edmonds, H.-Z. Tsai, *et al.*, Characterization of collective ground states in single-layer NbSe₂, *Nature Physics* **12**, 92 (2016).
- [34] J. Á. Silva-Guillén, P. Ordejón, F. Guinea, and E. Canadell, Electronic structure of 2H-NbSe₂ single-layers in the CDW state, *2D Materials* **3**, 035028 (2016).
- [35] F. Bischoff, W. Auwärter, J. V. Barth, A. Schiffrin, M. Fuhrer, and B. Weber, Nanoscale phase engineering of niobium diselenide, *Chemistry of Materials* **29**, 9907 (2017).
- [36] C. Chen, P. Das, E. Aytan, W. Zhou, J. Horowitz, B. Satpati, A. A. Balandin, R. K. Lake, and P. Wei, Strain-controlled superconductivity in few-layer NbSe₂, *ACS applied materials & interfaces* **12**, 38744 (2020).
- [37] S. Nagata, T. Aochi, T. Abe, S. Ebisu, T. Hagino, Y. Seki, and K. Tsutsumi, Superconductivity in the layered compound 2H-TaS₂, *Journal of Physics and Chemistry of Solids* **53**, 1259 (1992).
- [38] B. Sipoš, A. F. Kusmartseva, A. Akrap, H. Berger, L. Forró, and E. Tutiš, From Mott state to superconductivity in 1T-TaS₂, *Nature materials* **7**, 960 (2008).
- [39] E. Navarro-Moratalla, J. O. Island, S. Manas-Valero, E. Pinilla-Cienfuegos, A. Castellanos-Gomez, J. Quereda, G. Rubio-Bollinger, L. Chirolli, J. A. Silva-Guillén, N. Agrait, *et al.*, Enhanced superconductivity in atomically thin TaS₂, *Nature communications* **7**, 11043 (2016).
- [40] A. W. Tsen, R. Hovden, D. Wang, Y. D. Kim, J. Okamoto, K. A. Spoth, Y. Liu, W. Lu, Y. Sun, J. C. Hone, *et al.*, Structure and control of charge density waves in two-dimensional 1T-TaS₂, *Proceedings of the National Academy of Sciences* **112**, 15054 (2015).
- [41] T. Kumakura, H. Tan, T. Handa, M. Morishita, and H. Fukuyama, Charge density waves and superconductivity in 2H-TaSe₂, *Czechoslovak Journal of Physics* **46**, 2611 (1996).
- [42] N. Smith, S. Kevan, and F. DiSalvo, Band structures of the layer compounds 1T-TaS₂ and 2H-TaSe₂ in the presence of commensurate charge-density waves, *Journal of Physics C: Solid State Physics* **18**, 3175 (1985).
- [43] H. Ryu, Y. Chen, H. Kim, H.-Z. Tsai, S. Tang, J. Jiang, F. Liou, S. Kahn, C. Jia, A. A. Omrani, *et al.*, Persistent charge-density-wave order in single-layer TaSe₂, *Nano letters* **18**, 689 (2018).
- [44] C.-S. Lian, C. Heil, X. Liu, C. Si, F. Giustino, and W. Duan, Coexistence of superconductivity with enhanced charge density wave order in the two-dimensional limit of TaSe₂, *The Journal of Physical Chemistry Let-*

- ters **10**, 4076 (2019).
- [45] A. F. Kemper, B. Moritz, J. K. Freericks, and T. P. Devereaux, Theoretical description of high-order harmonic generation in solids, *New Journal of Physics* **15**, 023003 (2013).
- [46] C. R. McDonald, G. Vampa, G. Orlando, P. B. Corkum, and T. Brabec, Theory of high-harmonic generation in solids, *Journal of Physics: Conference Series* **594**, 012021 (2015).
- [47] T. T. Luu and H. J. Wörner, High-order harmonic generation in solids: A unifying approach, *Physical Review B* **94**, 115164 (2016).
- [48] M. Wu, D. A. Browne, K. J. Schafer, and M. B. Gaarde, Multilevel perspective on high-order harmonic generation in solids, *Physical Review A* **94**, 063403 (2016).
- [49] S. Ghimire and D. A. Reis, High-harmonic generation from solids, *Nature Physics* **15**, 10 (2019).
- [50] C. Yu, S. Jiang, and R. Lu, High order harmonic generation in solids: a review on recent numerical methods, *Advances in Physics: X* **4**, 1562982 (2019).
- [51] J. Park, A. Subramani, S. Kim, and M. F. Ciappina, Recent trends in high-order harmonic generation in solids, *Advances in Physics: X* **7**, 2003244 (2022).
- [52] L. Yue and M. B. Gaarde, Introduction to theory of high-harmonic generation in solids: tutorial, *Journal of the Optical Society of America B* **39**, 535 (2022).
- [53] H. Liu, Y. Li, Y. S. You, S. Ghimire, T. F. Heinz, and D. A. Reis, High-harmonic generation from an atomically thin semiconductor, *Nature Physics* **13**, 262 (2017).
- [54] G. Le Breton, A. Rubio, and N. Tancogne-Dejean, High-harmonic generation from few-layer hexagonal boron nitride: Evolution from monolayer to bulk response, *Physical Review B* **98**, 165308 (2018).
- [55] N. Tancogne-Dejean and A. Rubio, Atomic-like high-harmonic generation from two-dimensional materials, *Science Advances* **4**, eaao5207 (2018).
- [56] G. P. Zhang, M. S. Si, M. Murakami, Y. H. Bai, and T. F. George, Generating high-order optical and spin harmonics from ferromagnetic monolayers, *Nature Communications* **9**, 3031 (2018).
- [57] C. Liu, Y. Zheng, Z. Zeng, and R. Li, Polarization-resolved analysis of high-order harmonic generation in monolayer MoS₂, *New Journal of Physics* **22**, 073046 (2020).
- [58] J. Cao, F. Li, Y. Bai, P. Liu, and R. Li, Inter-half-cycle spectral interference in high-order harmonic generation from monolayer MoS₂, *Optics Express* **29**, 4830 (2021).
- [59] M. S. Mrudul and G. Dixit, High-harmonic generation from monolayer and bilayer graphene, *Physical Review B* **103**, 094308 (2021).
- [60] A. R. Khan, L. Zhang, K. Ishfaq, A. Ikram, T. Yildirim, B. Liu, S. Rahman, and Y. Lu, Optical harmonic generation in 2d materials, *Advanced Functional Materials* **32**, 2105259 (2022).
- [61] L. Yue, R. Hollinger, C. B. Uzundal, B. Nebgen, Z. Gan, E. Najafidehaghani, A. George, C. Spielmann, D. Kartashov, A. Turchanin, D. Y. Qiu, M. B. Gaarde, and M. Zuerch, Signatures of multiband effects in high-harmonic generation in monolayer mos₂, *Phys. Rev. Lett.* **129**, 147401 (2022).
- [62] A. Jimenez-Galan, C. Bossaer, G. Ernotte, A. M. Parks, R. E. F. Silva, D. M. Villeneuve, A. Staudte, T. Brabec, A. Luican-Mayer, and G. Vampa, Orbital perspective on high-harmonic generation from solids, *Nature Communica-*
- tions* **14**, 8421 (2023).
- [63] D. Zakhidov, D. A. Rehn, E. J. Reed, and A. Salleo, Reversible electrochemical phase change in monolayer to bulk-like MoTe₂ by ionic liquid gating, *ACS nano* **14**, 2894 (2020).
- [64] E. J. Sie, C. M. Nyby, C. Pemmaraju, S. J. Park, X. Shen, J. Yang, M. C. Hoffmann, B. Ofori-Okai, R. Li, A. H. Reid, *et al.*, An ultrafast symmetry switch in a Weyl semimetal, *Nature* **565**, 61 (2019).
- [65] H. Liu, Y. Li, Y. S. You, S. Ghimire, T. F. Heinz, and D. A. Reis, High-harmonic generation from an atomically thin semiconductor, *Nature Physics* **13**, 262 (2017).
- [66] C. P. Schmid, L. Weigl, P. Grössing, V. Junk, C. Gorini, S. Schlauderer, S. Ito, M. Meierhofer, N. Hofmann, D. Afanasiev, *et al.*, Tunable non-integer high-harmonic generation in a topological insulator, *Nature* **593**, 385 (2021).
- [67] S. A. Sato, K. Yabana, Y. Shinohara, T. Otobe, and G. F. Bertsch, Numerical pump-probe experiments of laser-excited silicon in nonequilibrium phase, *Phys. Rev. B* **89**, 064304 (2014).
- [68] A. Gomez Pueyo, M. A. Marques, A. Rubio, and A. Castro, Propagators for the time-dependent Kohn–Sham equations: Multistep, Runge–Kutta, exponential Runge–Kutta, and commutator free magnus methods, *Journal of chemical theory and computation* **14**, 3040 (2018).
- [69] K. Yabana, T. Sugiyama, Y. Shinohara, T. Otobe, and G. Bertsch, Time-dependent density functional theory for strong electromagnetic fields in crystalline solids, *Physical Review B* **85**, 045134 (2012).
- [70] S. A. Sato and K. Yabana, Maxwell+TDDFT multiscale simulation for laser-matter interactions, *Journal of Advanced Simulation in Science and Engineering* **1**, 98 (2014).
- [71] I. Floss, C. Lemell, G. Wachter, V. Smejkal, S. A. Sato, X.-M. Tong, K. Yabana, and J. Burgdörfer, Ab initio multiscale simulation of high-order harmonic generation in solids, *Physical Review A* **97**, 011401 (2018).
- [72] G. G. Brown, A. Jimenez-Galan, R. E. F. Silva, and M. Ivanov, Real-space perspective on dephasing in solid-state high harmonic generation, *Physical Review Research* **6**, 043005 (2024).
- [73] H. K. Avetissian and G. F. Mkrtchian, High laser harmonics induced by the Berry curvature in time-reversal invariant materials, *Physical Review B* **102**, 245422 (2020).
- [74] E. Runge and E. K. Gross, Density-functional theory for time-dependent systems, *Physical review letters* **52**, 997 (1984).
- [75] C. A. Ullrich, *Time-dependent density-functional theory: concepts and applications* (OUP Oxford, 2011).
- [76] K. Yabana, T. Nakatsukasa, J.-I. Iwata, and G. Bertsch, Real-time, real-space implementation of the linear response time-dependent density-functional theory, *physica status solidi (b)* **243**, 1121 (2006).
- [77] A. Castro, M. A. Marques, and A. Rubio, Propagators for the time-dependent Kohn–Sham equations, *The Journal of chemical physics* **121**, 3425 (2004).
- [78] A. Schleife, E. W. Draeger, Y. Kanai, and A. A. Correa, Plane-wave pseudopotential implementation of explicit integrators for time-dependent Kohn–Sham equations in large-scale simulations, *The Journal of chemical physics* **137** (2012).

- [79] D. A. Rehn, Y. Shen, M. E. Buchholz, M. Dubey, R. Namburu, and E. J. Reed, ODE integration schemes for plane-wave real-time time-dependent density functional theory, *The Journal of chemical physics* **150** (2019).
- [80] S. Meng and E. Kaxiras, Real-time, local basis-set implementation of time-dependent density functional theory for excited state dynamics simulations, *The Journal of Chemical Physics* **129**, 054110 (2008).
- [81] C. Pemmaraju, F. Vila, J. Kas, S. Sato, J. Rehr, K. Yabana, and D. Prendergast, Velocity-gauge real-time TDDFT within a numerical atomic orbital basis set, *Computer Physics Communications* **226**, 30 (2018).
- [82] K. Krieger, J. Dewhurst, P. Elliott, S. Sharma, and E. Gross, Laser-induced demagnetization at ultrashort time scales: Predictions of TDDFT, *Journal of chemical theory and computation* **11**, 4870 (2015).
- [83] The Elk Code, <http://elk.sourceforge.net/>.
- [84] M. A. Marques, A. Castro, G. F. Bertsch, and A. Rubio, octopus: a first-principles tool for excited electron-ion dynamics, *Computer Physics Communications* **151**, 60 (2003).
- [85] M. Noda, S. A. Sato, Y. Hirokawa, M. Uemoto, T. Takeuchi, S. Yamada, A. Yamada, Y. Shinohara, M. Yamaguchi, K. Iida, I. Floss, T. Otobe, K.-M. Lee, K. Ishimura, T. Boku, G. F. Bertsch, K. Nobusada, and K. Yabana, SALMON: Scalable Ab-initio Light-Matter simulator for Optics and Nanoscience, *Computer Physics Communications* **235**, 356 (2019).
- [86] K. Yabana and G. Bertsch, Time-dependent local-density approximation in real time, *Physical Review B* **54**, 4484 (1996).
- [87] M. Fuchs and M. Scheffler, Ab initio pseudopotentials for electronic structure calculations of poly-atomic systems using density-functional theory, *Computer Physics Communications* **119**, 67 (1999).
- [88] N. Troullier and J. L. Martins, Efficient pseudopotentials for plane-wave calculations, *Phys. Rev. B* **43**, 1993 (1991).
- [89] B. Riccò, Density of states of layer compounds. 2H-NbSe₂, *physica status solidi (b)* **77**, 287 (1976).
- [90] Y. Nakata, K. Sugawara, S. Ichinokura, Y. Okada, T. Hitosugi, T. Koretsune, K. Ueno, S. Hasegawa, T. Takahashi, and T. Sato, Anisotropic band splitting in monolayer NbSe₂: implications for superconductivity and charge density wave, *npj 2D Materials and Applications* **2**, 12 (2018).
- [91] S. Curtarolo, W. Setyawan, G. L. Hart, M. Jahnatek, R. V. Chepulskii, R. H. Taylor, S. Wang, J. Xue, K. Yang, O. Levy, *et al.*, AFLOW: An automatic framework for high-throughput materials discovery, *Computational Materials Science* **58**, 218 (2012).
- [92] F. Kadijk and F. Jellinek, On the polymorphism of niobium diselenide, *Journal of the Less Common Metals* **23**, 437 (1971).
- [93] C. G. Broyden, A class of methods for solving nonlinear simultaneous equations, *Mathematics of computation* **19**, 577 (1965).